Direct Measurement of Solid-Liquid Interfacial Energy Using a Meniscus

Jingcheng Ma,[1,*,†,§] Ishrat Zarin,[1,*] and Nenad Miljkovic[1,2,3,4,‡]
[1]Department of Mechanical Science and Engineering, University of Illinois, Urbana, 61801 Illinois, USA
[2]Materials Research Laboratory, University of Illinois, Urbana, 61801 Illinois, USA
[3]Department of Electrical and Computer Engineering, University of Illinois, Urbana, 61801 Illinois, USA
[4]International Institute for Carbon Neutral Energy Research (WPI-I2CNER), Kyushu University, 744 Motooka, Nishi-ku, Fukuoka 819-0395, Japan

(Received 5 May 2022; accepted 18 November 2022; published 9 December 2022)

Solid-liquid interactions are central to diverse processes. The interaction strength can be described by the solid-liquid interfacial free energy (γ_{SL}), a quantity that is difficult to measure. Here, we present the direct experimental measurement of γ_{SL} for a variety of solid materials, from nonpolar polymers to highly wetting metals. By attaching a thin solid film on top of a liquid meniscus, we create a solid-liquid interface. The interface determines the curvature of the meniscus, analysis of which yields γ_{SL} with an uncertainty of less than 10%. Measurement of classically challenging metal-water interfaces reveals $\gamma_{SL} \sim 30$–60 mJ/m^2, demonstrating quantitatively that water-metal adhesion is 80% stronger than the cohesion energy of bulk water, and experimentally verifying previous quantum chemical calculations.

DOI: 10.1103/PhysRevLett.129.246802

The interaction between a solid and liquid is essential to many fields [1–3]. Human wellness benefits from understanding of cellular behavior in complex biofluids [4,5]. The soil and crops in our environment respond to the absorption of rain and agricultural sprays [6]. In energy systems, the affinity of a solid to the working fluid determines the efficiency of boiling and condensation [7,8]. Within fuel cells and batteries, the electric double layer made up of water molecules near a metal electrode plays a key role in the electrochemistry [9]. To quantitatively describe these solid-liquid interfaces and interactions, the solid-liquid interfacial free energy (γ_{SL}) is used. This free energy arises from the imbalanced force on the liquid surface molecules that are attracted by the solid atoms on one side, and by the bulk liquid on the other side [10].

Although vital to many processes, the direct and accurate measurement of γ_{SL} remains a challenge. The most widely used approach to determine γ_{SL} is the liquid droplet contact angle technique [11,12], which was first introduced in the 1960s [13]. When a liquid droplet is in contact with a chemically homogeneous and smooth solid surface, it shows partial wetting and forms a spherical liquid cap, enabling the estimation of γ_{SL} from the measured droplet contact angle [13]. Although this method works well for soft and low-surface-energy materials such as polymers, it is not applicable for high-energy surfaces like metals, ceramics, or semiconductors, because the droplet spreads and eliminates the ability to measure a finite contact angle [14].

Here, in contrast with the classical approach of probing a droplet, we instead probe a liquid meniscus to directly measure γ_{SL} of a solid surface. We develop the solid-liquid interface by using the following steps. We first let a vertically suspended plate touch a liquid surface and allow a liquid meniscus to form. We then attach a thin and smooth solid film on this liquid meniscus, thus creating a solid-liquid interface that replaces the original liquid-air interface [Figs. 1(a) and 1(b)]. Herein, we define this meniscus as the multilayer solid-liquid meniscus (SL meniscus) to help differentiate it from a liquid meniscus which describes a free-liquid surface. The curvature of the SL meniscus changes when compared to a free water meniscus, which is caused by the solid-liquid interfacial interaction, and which enables the measurement of γ_{SL} from analysis of the meniscus profile [Fig. 1(c)].

The SL meniscus is similar to the well-studied liquid-air meniscus [15]. The shape of liquid meniscus formed on an adjacent vertical solid wall is determined by the equilibrium between the capillary force and the gravitational force. Immediately beneath the meniscus, the Laplace's pressure is equal to the hydrostatic pressure [15]:

$$\rho g y = \sigma_l \kappa_l = -\sigma_l \frac{\ddot{y}(x)}{\left[1 + \dot{y}(x)^2\right]^{1.5}}, \tag{1}$$

where y is the height of the liquid surface above the level of the liquid bath, x is the distance from the vertical wall, ρ is the liquid density, g is gravitational acceleration, κ_l is the meniscus curvature, and σ_l is liquid-vapor surface tension. The Laplace pressure is only contributed to by the principal curvature in the x-y plane. No curvature exists in the orthogonal y-z plane.

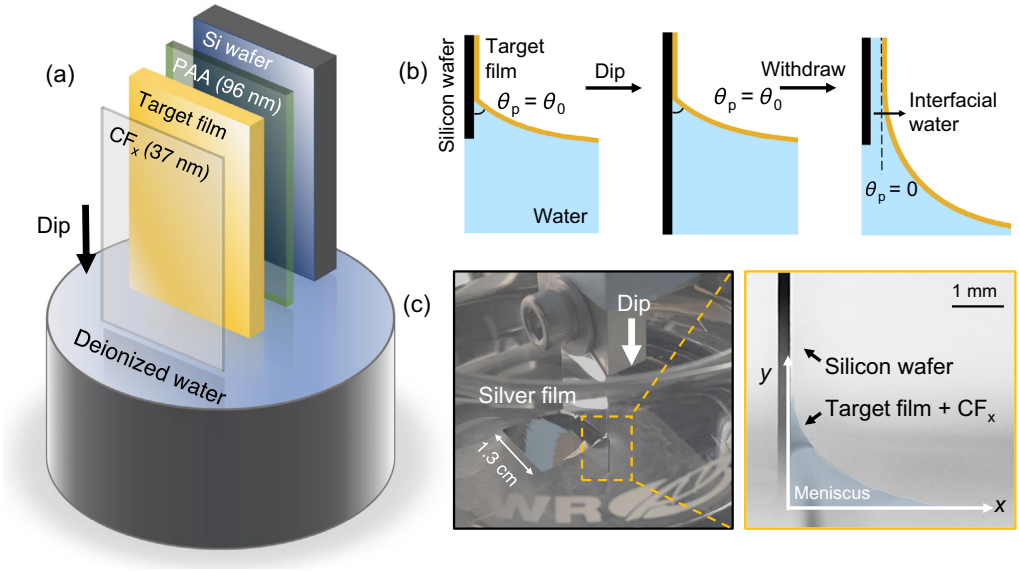

FIG. 1. Illustration of the measurement procedure. (a) Schematic diagram of the four-layer sample structure. (b) Schematic diagram of the sample dipping procedure that forms the peeling angle $\theta_p = 0$. (c) Optical images of the experimental setup and the side view of a silver-water meniscus.

For the SL meniscus, the Laplace pressure originates from the solid-liquid interface; hence, the surface tension term in Eq. (1) (σ_l) needs to be replaced by solid-liquid interfacial tension (σ_{SL}). The geometry of the SL meniscus is, therefore, described by

$$\rho g y = \sigma_{\mathrm{SL}} \kappa_{\mathrm{SL}}, \tag{2}$$

where κ_{SL} is the SL-meniscus curvature. Measuring the profile of a SL meniscus allows us to determine σ_{SL}, and sequentially γ_{SL}. We note that the interfacial tension σ_{SL}, which we directly measure, is not always numerically equal to γ_{SL}. Elastic stretching of the solid film also contributes to σ_{SL}. However, the elastic contribution is negligible in our rationally designed thin films system (<0.1 mJ/m^2) (see Sec. S2 of the Supplemental Material [16]).

It is critical to make the solid films sufficiently thin for the described measurement. This ensures that the bending energy (ε_b) is negligible when compared to the meniscus gravitational potential (ε_g). Otherwise, the elasticity of the solid film may change the shape of the meniscus. For soft materials having elastic moduli $E < 1$ GPa, the bending energy becomes significant ($>10^{-2}\varepsilon_\gamma$) when the solid film thickness $h > 100$ μm. For metals, the critical solid film thickness is $h \sim 1$ μm. Detailed analyses of ε_b and ε_g are included in Sec. S5 of the Supplemental Material [16].

We obtain the SL meniscus by fabricating a four-layer structured sample [Fig. 1(a)]. We used a 2-cm-long, 1.3-cm-wide, and 0.28-mm-thick polished silicon wafer as our substrate. A 96-nm-thick, water-soluble polyacrylic acid (PAA) film is first spun coat on the silicon wafer to act as a sacrificial layer. The target solid film is then deposited on the PAA film. Upon dipping the sample vertically into water, the PAA layer dissolves, and the target film is released and flows on top of the formed liquid meniscus. We found that the PAA film dissolves completely after 30 sec of water immersion, and the small amount of acrylic acid contamination does not affect the measurement (see Sec. S5 of the Supplemental Material [16]). Since the interface is not exposed to the ambient environment prior to the measurement, we avoid potential contamination from oxidation or volatile organic contamination [34–37]. On the top layer, we deposit a 37-nm-thick fluoropolymer coating to ensure that water flows into the interface to initiate meniscus formation, instead of flowing on top of the sample. Details of the materials fabrication and characterization are included in Sec. S1 of the Supplemental Material [16].

The peeling angle at the peeling front also governs the meniscus cross-sectional profile and affects data collection [θ_p; see Fig. 1(b)] [15,38,39]. We experimentally ensure that $\theta_p = 0$ every time so the meniscus profile solely depends on γ_{SL}. The front angle is determined by $\cos(\theta_p) = 1 - (G_w/\gamma_{\mathrm{SL}})$ [38,39], where G_w is the wet film-substrate adhesion. We first dip the sample into the liquid to a depth of 1.5 cm from the leading edge, then withdraw it by 5 mm, leaving a thin layer (~100 μm thick; see Supplemental Material, Fig. S8 [16]) of residual liquid in between the film and the substrate [Fig. 1(b)]. In this case, the wet adhesion to separate the film and substrate is 0; hence, $\cos(\theta_p) = 1$.

The meniscus profile is described by the analytical solution of Eq. (2), expressed as [15]

$$x_{\mathrm{exp}} - \Delta x = l_c' \cosh^{-1}\left(\frac{2l_c'}{y_{\mathrm{exp}} + \Delta y}\right) - 2l_c'\sqrt{1 - \frac{(y_{\mathrm{exp}} + \Delta y)^2}{4l_c'^2}}, \tag{3}$$

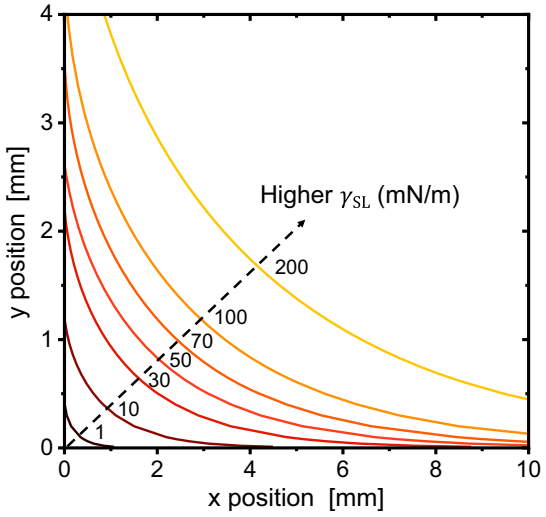

FIG. 2. Theoretically calculated [Eq. (3)] menisci x-y profiles for a variety of γ_{SL} when $\theta_p = 0$.

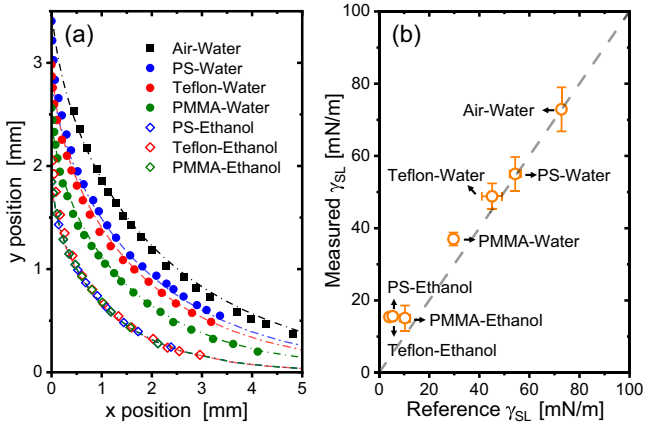

FIG. 3. Benchmarking using polymer-liquid interfaces. (a) Comparison between experimental measured (dots) and theoretically calculated (dashed lines) film menisci profiles. Error bars in position are smaller than the symbol size and are not shown. (b) Comparison between the results obtained using the SL-meniscus method (y axis) and contact angle method (x axis).

where $l_c' = \sqrt{\gamma_{SL}/\rho g}$ is the modified capillary length. The x-axis position parameter (Δx) can be determined using the boundary condition $\theta_p = 0$. A y-axis position parameter (Δy) is introduced because accurately determining $y = 0$ within a ± 0.1 mm uncertainty is difficult due to the blurry liquid surface. Therefore, we defined the vertical position of the lowest data point as $y_{exp} = 0$, and the real vertical position y to be $y = y_{exp} + \Delta y$, where Δy is fitted (typically $\Delta y = 10^{-5}$–10^{-4} m). The experimental dataset is fitted by the model of Eq. (3) to derive γ_{SL}. The theoretically calculated profiles of SL menisci for a variety of γ_{SL} are shown in Fig. 2. We estimate the uncertainty based on the goodness of fit and a 95% confidence interval in the parameter space of γ_{SL} and Δy. All fitting in our experiments have a coefficient of determination $R^2 > 0.99$, with uncertainty of γ_{SL} within 5%–10%. Accurate determination of Δy can further lower the uncertainty in γ_{SL}.

We benchmark our measurement technique using well-characterized nonpolar amorphous polymers, including polystyrene (PS, 199 nm thick), Teflon-AF (59 nm thick), and polymethylmethacrylate (PMMA, 170 nm thick). The nonpolar nature of these solids makes it convenient to establish reference values of γ_{SL} using classical Fowkes theory, which describes the solid surface free energy (γ_s) as being composed of the dispersive component ($\gamma_{s,d}$) and the polar component ($\gamma_{s,p}$): $\gamma_s = \gamma_{s,d} + \gamma_{s,p}$ [13]. The interfacial free energy is given by [13]

$$\gamma_{SL} = \gamma_s + \gamma_l - 2(\gamma_{s,d}\gamma_{l,d})^{0.5} - 2(\gamma_{s,p}\gamma_{l,p})^{0.5}, \quad (4)$$

where the surface energies of solids (γ_s) are measured by contact angle approach [40]. The surface energies of the liquids (γ_l) are obtained from the literature. See Sec. S2 of the Supplemental Material for additional surface energy analysis details [16].

Measurement on the free water meniscus (without any film) yielded $\gamma_l = 72.9 \pm 5.9$ mJ/m^2, consistent with the surface tension of water at room temperature $\sigma_l \approx$ 73 mN/m. For the polymer benchmarks, we did not use the sacrificial layer because capillary peeling can spontaneously occur due to the low polymer-silicon adhesion [38]. Other than water ($\gamma_{l,d} = 21.0$ mJ/m^2, $\gamma_{l,p} = 51.8$ mJ/m^2), we also used ethanol ($\gamma_{l,d} = 18.8$ mJ/m^2, $\gamma_{l,p} = 2.3$ mJ/m^2) to probe low γ_{SL} systems. The profiles of all seven menisci are shown in Fig. 3(a), where dashed lines represent lines of best fit. As predicted, the meniscus profile clearly depends on the chemistry of different solid films and testing liquids. A direct comparison between the reference γ_{SL} values and our measurements is included in Fig. 3(b), demonstrating good agreement. The polymer-ethanol interfaces showed lower γ_{SL} (<20 mJ/m^2) when compared to polymer-water interfaces, as predicted. However, the measured γ_{SL} for polymer-ethanol interfaces were 5–10 mJ/m^2 higher when compared to Fowkes theory. We hypothesize that charge transfer occurs at the ethanol-polymer interface, similar to past observations at the water-hydrocarbon interface [41], causing ethanol molecule orientation to deviate from its bulk orientation, and sequentially making the liquid near the surface more polar. Images of all measured menisci are included in Sec. S3 of the Supplemental Material [16].

We now demonstrate the capability of our technique to measure highly wetting and rigid materials. We measure γ_{SL} between water and five sputtered metallic films, including inert metal films: gold (180 ± 3 nm thick), silver (176 ± 4 nm thick), platinum (206 ± 3 nm thick), and noninert metals including aluminum (172 ± 6 nm thick) and titanium (161 ± 6 nm thick). The measured profiles are included in Fig. 4(a). The metals were deposited on the PAA surfaces by magnetron sputtering (see Sec. S1 of the

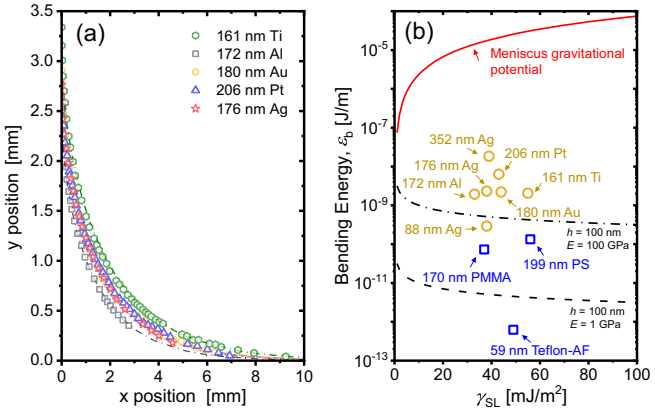

FIG. 4. Measurements on water-metal interfaces. (a) Comparison between experiment (data points) and best fit (dashed lines) of the film meniscus profiles. (b) Thin film bending energy (ε_b) as a function of γ_{SL}. Data points represent samples used in our experiments, and the black dashed lines are theoretical values for 100-nm-thick polymer ($E = 1$ GPa) and metal ($E = 100$ GPa) films. The meniscus gravitational potential (ε_g, red solid line) is also included for comparison.

Supplemental Material [16]). The mechanical bending of the metal films having thickness of ~100 nm is not expected to affect the accuracy of the γ_{SL} measurement. Figure 4(b) shows the bending energy (ε_b) of all films used. When compared to the gravitational potential energy (red solid line), ε_b are all negligible ($<10^{-3}\varepsilon_g$). We also did not observe possible measurement deviations from inclusion of the PAA layer (see Sec. S4 of the Supplemental Material [16]).

The measured γ_{SL} of all metal-water interfaces ranged from 30 to 60 mJ/m^2. Unexpectedly, they are comparable to the measurement results of the polymer-water interfaces (~50 mJ/m^2), even though the metal surfaces should interact differently with water. We interpret this result as arising from the imbalanced molecular forces between the interfacial water and its bulk. Despite the interfacial water adhering poorly with nonpolar polymers and binding strongly with clean metals [2,42], the interfacial molecular forces are comparably imbalanced with respect to the bulk water hydrogen bonds, resulting in similar γ_{SL} values. The minimum γ_{SL} value is 0 and can be found in between polymers and metals when the solid polarity is waterlike, where the molecular forces are perfectly balanced. Therefore, we infer that γ_{SL} for most solids and water is lower than 70 mJ/m^2.

Our measurements provide useful insights into the metal-water interface. Here, we provide two brief discussions on the metal surface energy and mesoscopic wettability, as well as the estimation of the strength of the metal-water hydrogen bond. The mesoscopic wettability of metals, which closely relates to the surface energy of a metal, has been a topic of controversy in the past [12,13,43,44]. Because of complete wetting of water on

TABLE I. Measured values of γ_{SL}, $\gamma_{s,p}$, and G_{SL} at the polymer-water and metal-water interfaces. Uncertainties of $\gamma_{s,p}$ and G_{SL} were computed using propagation of error.

Solid material	Solid-water interfacial free energy γ_{SL} (mJ/m^2)	Solid polar surface energy $\gamma_{s,p}$ (mJ/m^2)	Solid-water adhesion G_{SL} (mJ/m^2)
Teflon-AF	48.8 ± 3.6	0.1 ± 0.1	33.2 ± 1.7
PS	56.0 ± 4.6	0.0 ± 0.7	59.0 ± 4.7
PMMA	37.1 ± 1.8	16.4 ± 3.4	93.8 ± 4.1
Gold	43.5 ± 2.3	176.2 ± 5.0	255.8 ± 5.6
Silver	38.2 ± 3.1	164.5 ± 7.0	249.4 ± 7.7
Platinum	42.6 ± 1.4	174.7 ± 3.0	254.7 ± 3.3
Aluminum	32.5 ± 1.4	152.6 ± 3.3	241.6 ± 3.6
Titanium	56.2 ± 1.6	202.9 ± 3.2	269.4 ± 3.6

metals, the exact magnitude of surface energy of a metal γ_s cannot be obtained from the contact angle measurement. Some estimate it to be almost zero [43,44] while others claim it to be ~10^3 mJ/m^2 [45]. Here, we obtain the apparent γ_s at water interface using our measured γ_{SL} in combination with Eq. (4).

For all metals studied here, $\gamma_{s,d} \approx 50$ mJ/m^2 as measured using the contact angle approach with a nonpolar probe fluid diiodomethane (see Sec. S2 of the Supplemental Material [16]). Sequentially, the polar surface energy $\gamma_{s,p}$ of our metals can be obtained, which ranged from 150 to 200 mJ/m^2 (see Table I). This result indicates that metals are highly polar when compared to ceramics and polymers. The measured $\gamma_{s,p}$ values for metals are consistent with conventional wisdom that clean metals are intrinsically hydrophilic from analysis of the Young-Dupre equation: $\cos\alpha = (\gamma_s - \gamma_{SL})/\gamma_l > 1$, where α is the water droplet apparent contact angle. This result ($\cos\alpha > 1$) indicates that the droplet fully spreads on the solid; hence, the Young-Dupre equation fails to describe the shape of the droplet. Based on this result, we note that previous works describing clean metals as nonpolar owing to delocalization of electrons may not be correct [13,44]. See Sec. S7 of the Supplemental Material for additional discussion and comparison with past literature [16]. We also note that recent simulations have revealed that clean metals can appear to be hydrophobic due to the presence of a surface water bilayer closely bonded with the metal surface, leaving no active hydrogen bonds with bulk water [43]. Although the γ_{SL} we measure can indeed be interpreted in this way (see Sec. S7 of the Supplemental Material [16]), such hydrophobicity is expected of surfaces having well-controlled chemistry and crystal orientation and is unlikely to occur on our sputtered metal surfaces. Examining such effects requires careful control of the surface down to the atomic level.

Our measurements of γ_{SL} also provide insights on the strength of water-metal adhesion, which is mainly

governed by metal-water hydrogen bonds. We calculated the water-metal adhesion (G_{SL}) using classical thermodynamics $G_{SL} = \gamma_s + \gamma_l - \gamma_{SL}$ [12,13], which yielded $G_{SL} =$ 240–270 mJ/m^2 at the metal-water interface (see Table I). This is consistent with simulations based on density functional theory (170–240 mJ/m^2) [46]]. This value is approximately 80% higher than the cohesion energy of water ($2\gamma_l \approx 140$ mJ/m^2) and 5–10 times higher than the polymer-water adhesion. Such high adhesion is expected from the strong water-metal hydrogen bonds between an icelike interfacial water bilayer on clean metals, as observed by ultrahigh vacuum experiments [1,2,42].

In addition to metals, our technique presented here can provide important benchmark measurements to understand a variety of solid-liquid interfaces, especially for stiff materials such as high-energy inorganic crystals where contact angle methods are not applicable. One limitation of our technique is the lack of general strategies to create the SL meniscus. Methods which can be applied to any material or working fluid system need further development. Capillary peeling works for a limited amount of interfaces [38]; hence, developing sacrificial layers for different probe liquids requires future investigation. Currently, the approach used to understand highly wetting solid-liquid interfaces relies on computational tools, including molecular dynamics simulations [47,48], density functional theory [1,3,49,50], and machine-learning models [35,51]. Direct experimental measurement of γ_{SL} provides valuable experimental datasets to optimize these computational tools, demonstrating a promising method to understand solid-liquid interfaces, and to enable reliable closed-loop design of materials and surfaces for numerous applications.

The authors thank Dr. David G. Cahill of the University of Illinois for the insightful discussions regarding surface stress. The authors gratefully acknowledge funding support from the Office of Naval Research (ONR) under Grant No. N00014-21-1-2089. N. M. gratefully acknowledges funding support from the International Institute for Carbon Neutral Energy Research (WPI-I2CNER), sponsored by the Japanese Ministry of Education, Culture, Sports, Science and Technology.

The authors declare no competing financial interests.

[*]These authors contributed equally to this work.
[†]Corresponding author.
jcma36@uchicago.edu
[‡]Corresponding author.
nmiljkov@illinois.edu
[§]Present address: The James Franck Institute, University of Chicago, Chicago, 60637 Illinois, USA.

[1] J. Carrasco, A. Hodgson, and A. Michaelides, A molecular perspective of water at metal interfaces, Nat. Mater. **11**, 667 (2012).
[2] P. A. Thiel and T. E. Madey, The interaction of water with solid surfaces: Fundamental aspects, Surf. Sci. Rep. **7**, 211 (1987).
[3] E. Bjornehohn, M. H. Hansen, A. Hodgson, L. M. Liu, D. T. Limmer, A. Michaelides, P. Pedevilla, J. Rossmeisl, H. Shen, G. Tocci, E. Tyrode, M. M. Walz, J. Werner, and H. Bluhm, Water at interfaces, Chem. Rev. **116**, 7698 (2016).
[4] K. L. Weirich, S. Banerjee, K. Dasbiswas, T. A. Witten, S. Vaikuntanathan, and M. L. Gardel, Liquid behavior of cross-linked actin bundles, Proc. Natl. Acad. Sci. U.S.A. **114**, 2131 (2017).
[5] Y. W. Jiang and B. Z. Tian, Inorganic semiconductor biointerfaces, Nat. Rev. Mater. **3**, 473 (2018).
[6] M. Damak, S. R. Mahmoudi, M. N. Hyder, and K. K. Varanasi, Enhancing droplet deposition through in-situ precipitation, Nat. Commun. **7**, 12560 (2016).
[7] J. B. Boreyko and C. H. Chen, Self-Propelled Dropwise Condensate on Superhydrophobic Surfaces, Phys. Rev. Lett. **103**, 184501 (2009).
[8] N. Miljkovic, R. Enright, and E. N. Wang, Effect of droplet morphology on growth dynamics and heat transfer during condensation on superhydrophobic nanostructured surfaces, ACS Nano **6**, 1776 (2012).
[9] S. Benaglia, M. R. Uhlig, J. Hernandez-Munoz, E. Chacon, P. Tarazona, and R. Garcia, Tip Charge Dependence of Three-Dimensional AFM Mapping of Concentrated Ionic Solutions, Phys. Rev. Lett. **127** (2021).
[10] A. F. M. Barton, in *Encyclopedia of Physical Science and Technology*, 3rd edition (Academic Press, 2003), pp. 233–251, 10.1016/B0-12-227410-5/00118-6.
[11] H. Cha, J. Ma, Y. S. Kim, L. N. Li, L. W. Sun, J. S. Tong, and N. Miljkoyic, In situ droplet microgoniometry using optical microscopy, ACS Nano **13**, 13343 (2019).
[12] F. M. Fowkes, Additivity of intermolecular forces at interfaces.1. Determination of contribution to surface and interfacial tensions of dispersion forces in various liquids, J. Phys. Chem. **67**, 2538 (1963).
[13] F. M. Fowkes, Attractive forces at interfaces, Ind. Eng. Chem. **56**, 40 (1964).
[14] D. Quere, Wetting and roughness, Annu. Rev. Mater. Res. **38**, 71 (2008).
[15] P.-G. De Gennes, F. Brochard-Wyart, and D. Quéré, *Capillarity and Wetting Phenomena: Drops, Bubbles, Pearls, Waves* (Springer Science & Business Media, New York, 2013), pp. 43–47.
[16] See Supplemental Material at http://link.aps.org/supplemental/10.1103/PhysRevLett.129.246802 for additional details, analysis, and discussions, which includes Refs. [17–33].
[17] X. Xie, K. X. Yang, D. Y. Li, T. H. Tsai, J. Shin, P. V. Braun, and D. G. Cahill, High and low thermal conductivity of amorphous macromolecules, Phys. Rev. B **95**, 035406 (2017).
[18] H. Grunewal, Weast, Rc—CRC handbook of chemistry and physics, Angew. Chem., Int. Ed. Engl. **5**, 907 (1966).
[19] Q. Xu, K. E. Jensen, R. Boltyanskiy, R. Sarfati, R. W. Style, and E. R. Dufresne, Direct measurement of strain-dependent solid surface stress, Nat. Commun. **8**, 555 (2017).

[20] R. Shuttleworth, The surface tension of solids, Proc. Phys. Soc. London Sect. A **63**, 444 (1950).
[21] E. Orowan, Surface energy and surface tension in solids and liquids, Proc. R. Soc. A **316**, 473 (1970).
[22] S. Mondal, M. Phukan, and A. Ghatak, Estimation of solid–liquid interfacial tension using curved surface of a soft solid, Proc. Natl. Acad. Sci. U.S.A. **112**, 12563 (2015).
[23] R. D. Schulman, M. Trejo, T. Salez, E. Raphael, and K. Dalnoki-Veress, Surface energy of strained amorphous solids, Nat. Commun. **9**, 982 (2018).
[24] F. M. Fowkes, Additivity of intermolecular forces at interfaces. I. Determination of the contribution to surface and interfacial tensions of dispersion forces in various liquids, J. Phys. Chem. **67**, 2538 (1963).
[25] H. Cha, J. Ma, Y. S. Kim, L. Li, L. Sun, J. Tong, and N. Miljkovic, In situ droplet microgoniometry using optical microscopy, ACS Nano **13**, 13343 (2019).
[26] Y. Zhang, M. T. Yin, Y. Baek, K. Lee, G. Zangari, L. H. Cai, and B. X. Xu, Capillary transfer of soft films, Proc. Natl. Acad. Sci. U.S.A. **117**, 5210 (2020).
[27] J. Rafiee, X. Mi, H. Gullapalli, A. V. Thomas, F. Yavari, Y. F. Shi, P. M. Ajayan, and N. A. Koratkar, Wetting transparency of grapheme, Nat. Mater. **11**, 217 (2012).
[28] E. M. Lifshitz, The theory of molecular attractive forces between solids, Sov. Phys. JETP **2**, 73 (1956).
[29] C. J. Van Oss, M. K. Chaudhury, and R. J. Good, Interfacial Lifshitz-van der Waals and polar interactions in macroscopic systems, Chem. Rev. **88**, 927 (1988).
[30] P. Tolias, Non-retarded room temperature Hamaker constants between elemental metals, Surf. Sci. **700**, 121652 (2020).
[31] P. J. Feibelman, G. A. Kimmel, R. S. Smith, N. G. Petrik, T. Zubkov, and B. D. Kay, A unique vibrational signature of rotated water monolayers on Pt(111): Predicted and observed, J. Chem. Phys. **134**, 204702 (2011).
[32] C. J. Shih, Q. H. Wang, S. C. Lin, K. C. Park, Z. Jin, M. S. Strano, and D. Blankschtein, Breakdown in the Wetting Transparency of Graphene, Phys. Rev. Lett. **109**, 176101 (2012); **115**, 049901(E) (2015).
[33] H. M. Lu and Q. Jiang, Surface tension and its temperature coefficient for liquid metals, J. Phys. Chem. B **109**, 15463 (2005).
[34] X. Yan, Z. Y. Huang, S. Sett, J. Oh, H. Cha, L. N. Li, L. Z. Feng, Y. F. Wu, C. Y. Zhao, D. Orejon, F. Chen, and N. Miljkovic, Atmosphere-mediated superhydrophobicity of rationally designed micro/nanostructured surfaces, ACS Nano **13**, 4160 (2019).
[35] R. Freitas and E. J. Reed, Uncovering the effects of interface-induced ordering of liquid on crystal growth using machine learning, Nat. Commun. **11**, 1496 (2020).
[36] J. Li, Y. Zhao, J. Ma, W. Fu, X. Yan, K. F. Rabbi, and N. Miljkovic, Superior antidegeneration hierarchical nanoengineered wicking surfaces for boiling enhancement, Adv. Funct. Mater. **32**, 2108836 (2021).
[37] D. J. Preston, N. Miljkovic, J. Sack, R. Enright, J. Queeney, and E. N. Wang, Effect of hydrocarbon adsorption on the wettability of rare earth oxide ceramics, Appl. Phys. Lett. **105**, 011601 (2014).
[38] J. Ma, J. M. Kim, M. J. Hoque, K. J. Thompson, S. Nam, D. C. Cahill, and N. Miljkovic, Role of thin film adhesion on capillary peeling, Nano Lett. **21**, 9983 (2021).
[39] S. Khodaparast, F. Boulogne, C. Poulard, and H. A. Stone, Water-Based Peeling of Thin Hydrophobic Films, Phys. Rev. Lett. **119**, 154502 (2017).
[40] J. C. Ma, D. G. Cahill, and N. Miljkovic, Condensation induced blistering as a measurement technique for the adhesion energy of nanoscale polymer films, Nano Lett. **20**, 3918 (2020).
[41] S. Pullanchery, S. Kulik, B. Rehl, A. Hassanali, and S. Roke, Charge transfer across C–H $\cdots$ O hydrogen bonds stabilizes oil droplets in water, Science **374**, 1366 (2021).
[42] H. Ogasawara, B. Brena, D. Nordlund, M. Nyberg, A. Pelmenschikov, L. G. M. Pettersson, and A. Nilsson, Structure and Bonding of Water on Pt(111), Phys. Rev. Lett. **89**, 276102 (2002).
[43] D. T. Limmer, A. P. Willard, P. Madden, and D. Chandler, Hydration of metal surfaces can be dynamically heterogeneous and hydrophobic, Proc. Natl. Acad. Sci. U.S.A. **110**, 4200 (2013).
[44] M. E. Schrader, Wettability of clean metal-surfaces, J. Colloid Interface Sci. **100**, 372 (1984).
[45] L. Vitos, A. V. Ruban, H. L. Skriver, and J. Kollar, The surface energy of metals, Surf. Sci. **411**, 186 (1998).
[46] S. Gim, K. J. Cho, H. K. Lim, and H. Kim, Structure, dynamics, and wettability of water at metal interfaces, Sci. Rep. **9**, 1 (2019).
[47] T. Y. Yin, D. Shin, J. Frechette, C. E. Colosqui, and G. Drazer, Dynamic Effects on the Mobilization of a Deposited Nanoparticle by a Moving Liquid-Liquid Interface, Phys. Rev. Lett. **121**, 238002 (2018).
[48] G. Srinivas, S. O. Nielsen, P. B. Moore, and M. L. Klein, Molecular dynamics simulations of surfactant self-organization at a solid-liquid interface, J. Am. Chem. Soc. **128**, 848 (2006).
[49] W. A. Curtin, Density-Functional Theory of the Solid-Liquid Interface, Phys. Rev. Lett. **59**, 1228 (1987).
[50] J. Y. Lu, Q. Y. Ge, H. X. Li, A. Raza, and T. J. Zhang, Direct Prediction of Calcite Surface Wettability with First-Principles Quantum Simulation, J. Phys. Chem. Lett. **8**, 5309 (2017).
[51] C. Schran, F. L. Thiemann, P. Rowe, E. A. Muller, O. Marsalek, and A. Michaelides, Machine learning potentials for complex aqueous made, Proc. Natl. Acad. Sci. U.S.A. **118**, e2110077118 (2021).